CrystEngComm

PAPER

View Article Online
View Journal | View Issue

Cite this: *CrystEngComm*, 2025, **27**, 4744

Chiral resolution of copper aspartate under reaction–diffusion: synergy of experiment and simulation†

Poh Ying Fong, [a] Sehrish Khan,[a] Hatem M. Titi, [b] Manal Ammar,[c] Fiorenzo Vetrone,[d] Mazen Al-Ghoul*[c] and Louis A. Cuccia *[a]

Chiral resolution is essential in the pharmaceutical and food industries and in materials science, due to the unique properties of enantiomers. Here, we investigate the coordination polymerization of homochiral (L- and D-) and racemic (DL-) copper aspartate (CuAsp), as well as the spatiotemporal resolution of racemic aspartic acid (DL-Asp) using L- and D-proline (Pro) as tailor-made additives (TMAs), all within the reaction–diffusion framework (RDF) in a quasi-one-dimensional (1D) agar gel system. We combine experimental approaches—leading to spherulitic CuAsp coordination polymers characterized by solid-state circular dichroism (CD), powder X-ray diffraction (PXRD), and thermal analyses—with a newly developed simulation model grounded in classical reaction–diffusion and Cahn–Hilliard equations. These numerical simulations reproduce the experimentally observed Liesegang banding and the chiral inversion phenomenon, where the earliest precipitates adopt the opposite handedness to the proline dopant, consistent with Harada's application of the 'rule of reversal'. Parameter choices in the model draw on Harada's original insights, capturing both racemic and chiral scenarios. The simulations confirm how slight adjustments to nucleation barriers and stability can account for increased solubility in enantiopure conditions and partial chiral switching in doped systems. Experimentally, CuAsp near the liquid–gel interface crystallizes in the opposite configuration of the TMA, while more distant regions show varied chirality due to concentration gradients. Overall, both experiment and simulation highlight how the RDF, combined with a modest chiral bias, offers a versatile method for effecting chiral resolution in conglomerate crystalline systems, with broad potential for enantioselective separation strategies.

Received 5th April 2025,
Accepted 7th June 2025

DOI: 10.1039/d5ce00376h

rsc.li/crystengcomm

Introduction

Coordination polymers (CPs) are versatile metal–ligand compounds that can form one-, two- or three-dimensional structures.[1,2] Their ability to incorporate various metals and ligands has led to a wide range of applications, including magnetism,[3] gas adsorption,[4] catalysis,[5] luminescence,[6] and drug delivery.[7] Recent advancements have focused on chiral CPs due to their complex architectures and potential in enantioselective separation and asymmetric catalysis.[2,8] The ideal enantiopure ligand should be accessible, cost-effective, environmentally friendly, and exhibit flexible coordination behavior.[2] Strategic selection and design of chiral ligands are crucial for developing multifunctional chiral CPs. Amino acids, in particular, have garnered significant attention for their efficient coordination with metal ions.[9–11] Their distinct amino, carboxylate, and side chain functional groups render them ideal for complexation.[12,13] Several research groups have demonstrated the fabrication of 1D nanostructures, such as nanofibers,[9,10,14] nanowires,[15] nanobelts,[16] and nanorods[11] from metal–amino acid assemblies. For example, Imaz *et al.* successfully prepared CuAsp nanofibers at the interface of a Cu^{2+} solution with a water/ethanol mixture containing deprotonated L- or D-Asp.[9] Similarly, Pu *et al.* and Wu *et al.* demonstrated the self-assembly of CuGlu,[10,17] CuAsp,[10] and CuAmi[10] at room temperature. Their studies revealed that crystallization is driven by coordination between deprotonated amino acids and Cu^{2+} metal ions in a proposed square planar coordination geometry. Furthermore, amino acid chirality influences supramolecular self-assembly.[10,17]

[a] *Department of Chemistry and Biochemistry, Concordia University, 7141 Sherbrooke Street West, H4B 1R6 Montreal, Canada. E-mail: sekha8@ulaval.ca, louis.cuccia@concordia.ca*
[b] *Department of Chemistry, McGill University, 801 Sherbrooke Street West, H3A 0B8 Montreal, Canada*
[c] *Department of Chemistry, American University of Beirut, P.O. Box 11-0236, Riad El-Solh, 1107 2020 Beirut, Lebanon. E-mail: mazen.ghoul@aub.edu.lb*
[d] *Centre Énergie, Matériaux et Télécommunications, Institut National de la Recherche Scientifique, Université du Québec, 1650 Boul. Lionel-Boulet, J3X 1P7 Varennes, Canada*

† Electronic supplementary information (ESI) available. See DOI: https://doi.org/10.1039/d5ce00376h

Chiral resolution is crucial in the pharmaceutical and food industries, where enantiopure products are essential.[18] Various techniques have been developed to resolve conglomerate crystalline systems,[19–23] with preferential crystallization (PC) being particularly effective in resolving conglomerate crystals by seeding a supersaturated solution with the preferred enantiomer.[20] Pioneering work by Kaoru Harada more than 50 years ago demonstrated the successful separation of DL-Asp, DL-Glu, and DL-Asn using homochiral amino acid-copper complexes.[24–27] Addadi *et al.* later introduced the 'rule of reversal' to rationalize how the enantiomer with the opposite configuration crystallizes preferentially in the presence of homochiral tailor-made additives (TMAs).[28] This inversion is not adequately explained by stereoselective ligand exchange alone. Harada's original experiments showed that, despite differences in ligand exchange rates between L- and D-aspartate, the configuration of the earliest precipitates reflected not kinetic preference, but rather differences in solubility, local supersaturation, and nucleation kinetics. At low additive-to-racemate ratios, the system favors the opposite enantiomer due to these subtle physicochemical effects. At higher additive concentrations, or later stages of crystallization, the preferred enantiomer can switch—leading to band-by-band enantiomeric alternation as observed in reaction–diffusion systems. Homochiral TMAs share a similar structure with the solute molecules, allowing for enantioselective adsorption, which in turn hinders nucleation and crystal growth of one enantiomer.[19,28–30] More recently, Kongsamai *et al.* explored the resolution of DL-Asn·H_2O using D-Asp and D-Glu,[31] while Gou *et al.* and Sun *et al.* reported higher product yields and purity of (*S*)-mandelic acid and L-norvaline, respectively, using PC with TMAs.[32,33] The reaction–diffusion framework (RDF) offers a robust platform for investigating chiral resolution and pattern formation in coordination polymers, functioning under far-from-equilibrium conditions.[34] In this framework, a metal ion such as Cu^{2+} diffuses through a gel medium containing a chiral ligand (homochiral or racemic), creating a dynamic concentration gradient. This gradient drives the nucleation and growth of coordination polymers, resulting in highly organized structures.[35,36] What distinguishes RDF is its ability to facilitate self-organization at multiple scales. While distinct patterns, such as Liesegang rings or spherulites, emerge at the macroscopic level, there is also concurrent self-organization at the microscopic scale, where molecular interactions dictate the arrangement of atoms within the coordination polymer.[35,37] This hierarchical self-organization is a hallmark of far-from-equilibrium systems, where the continuous influx of energy or matter drives complexity and order.[34]

One of the remarkable features of RDF-based self-organization is its capacity for selective spatial segregation. As the system evolves, distinct bands of precipitated material form in the gel.[37] This spatial organization not only allows for the segregation of particles based on size but also provides a strategy for attempting to segregate various chiral compounds into these bands. Through the careful control of reaction conditions, such as ion concentration and ligand chirality, this method may enable the separation of enantiomers *in situ*, as different chiral species preferentially nucleate and crystallize in specific bands. This capability opens new possibilities for chiral resolution and enantioselective separations in structured environments.

In the present study, the diffusion of Cu^{2+} into a gel matrix containing deprotonated aspartate ligand results in the formation of blue spherulites made of a coordination polymer of CuAsp. This process exemplifies self-organization across length scales, as the spherulites exhibit macroscopic symmetry, while the chiral nature of the ligands dictates their microscopic arrangement. The far-from-equilibrium nature of the RDF ensures that the system does not settle into a static, low-energy arrangement but instead continues to evolve,[38] allowing for the emergence of intricate spatial patterns and chiral resolution.

Inspired by the work of Imaz *et al.*[9] and Harada *et al.*,[27] this study aims to explore the chiral crystallization of L- and D-aspartate and the spatiotemporal resolution of DL-aspartate using homochiral additives in an agar gel medium. Harada's work focused on the chiral resolution of racemic aspartic acid using various copper-amino acid complexes under controlled conditions, revealing a phenomenon of "chiral inversion" in the earliest precipitates. Specifically, when L-proline was introduced, D-aspartate tended to crystallize first, while D-proline favored initial L-aspartate precipitation. This behavior could not be attributed solely to a simple ligand-exchange mechanism; instead, solubility differences and kinetic factors (including local complexation equilibria and diffusion-limited growth) emerged as critical contributors. As the reaction front advanced and dopant concentrations shifted, later-formed precipitates sometimes reverted to the same chirality as the proline additive, underscoring the dynamic nature of the enantiomeric composition over time. Through the application of the RDF, this work seeks to uncover new insights into the mechanisms driving chiral resolution and the role of amino acid chirality in the formation of coordination polymers. The findings contribute to the broader understanding of chiral materials design and the development of novel techniques for enantioselective separation in structured environments.

Results and discussion

Coordination polymerization and characterization of L-, D-, and DL-CuAsp in agar gel

Research on the coordination polymerization of CuAsp has traditionally focused on solution-based self-assembly processes.[9,10] However, to our knowledge, the coordination polymerization of CuAsp in hydrogels has yet to be reported. Taking advantage of the RDF, we successfully achieved the periodic precipitation (Liesegang banding) of L-, D-, and DL-CuAsp coordination polymers in a 1D agar gel system (Fig. 1). The diffusion of $Cu(NO_3)_2{\cdot}3H_2O$ solution, serving as

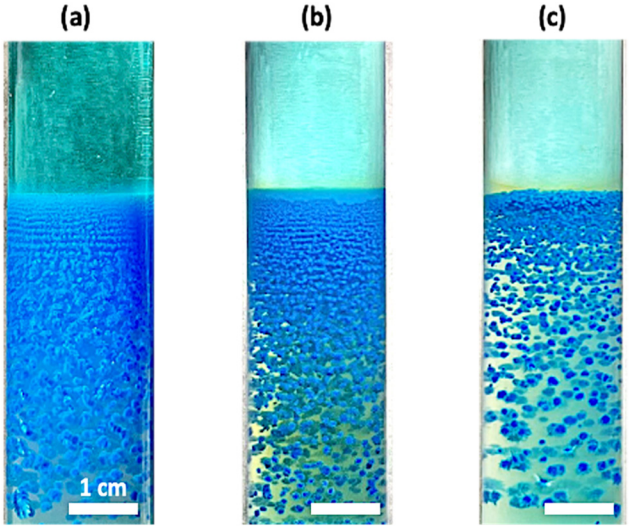

Fig. 1 Periodic precipitation of L-, D-, and DL-CuAsp coordination polymers in a 1% agar gel system. (a) L-CuAsp, (b) D-CuAsp, and (c) DL-CuAsp, showing distinct Liesegang banding patterns. The diffusion of $Cu(NO_3)_2{\cdot}3H_2O$ (outer electrolyte) into the gel containing deprotonated Asp (inner electrolyte) leads to the formation of blue CuAsp spherulites. The initial concentrations used were $[Cu^{2+}]$ = 300 mM in the outer electrolyte and [Asp] = 50 mM, [NaOH] = 100 mM in the inner electrolyte, with 1% agar as the gel matrix. The reaction was conducted at ~22 °C. The spatiotemporal evolution of the precipitation process is shown in Fig. S1.†

the outer electrolyte, into the gel containing deprotonated Asp led to the formation of distinct blue spherulites. The temporal evolution of this periodic precipitation is depicted in Fig. S1.†

A notable 6-fold higher concentration of Cu^{2+} outer electrolyte was used to create a high level of supersaturation at the liquid–gel interface, facilitating rapid diffusion.[35] This setup established a concentration gradient, where supersaturation decreased progressively with distance from the interface.[35] At the interface, the highest concentration of Cu^{2+} ions leads to rapid nucleation due to high supersaturation. Since nucleation dominates crystal growth at high supersaturation, many small spherulites form simultaneously, competing for available ions (Fig. 2a). This results in a high number of nuclei, limiting the growth of each crystal. Furthermore, in the middle zone, the supersaturation decreases as Cu^{2+} ions diffuse further from the liquid–gel interface. Here, nucleation slows down, allowing the spherulites that form to grow larger as crystal growth begins to dominate over nucleation. This creates a balance between nucleation and crystal growth, leading to intermediate particle sizes (Fig. 2a). When Cu^{2+} ions reach the bottom zone, supersaturation is significantly lower. Fewer nuclei form in this region, allowing the already formed spherulites to grow larger due to reduced ion competition. Crystal growth is the dominant process, leading to the formation of large spherulites (Fig. 2a).

Spherulite formation is a common phenomenon in RDFs.[39] It begins with the nucleation at a single point. Once nucleation occurs, anisotropic forces drive the directional growth of nanofibers of CuAsp coordination polymers away from the nucleus, resulting from the established concentration gradient. As the CuAsp nanofibers grow, they align radially from the nucleation site, with the diffusion flux continuing to supply material that contributes to the growth of the fibers. This results in the formation of bundles of nanofibers, where each bundle maintains a preferred orientation driven by the anisotropy in the reaction environment.[39] These nanofiber bundles progressively organize into a hierarchical structure, with the inner layers of the spherulite formed first, followed by the addition of outer layers as the reaction continues. The hierarchical organization is a crucial feature of spherulitic growth, where small-scale units such as nanofibers are integrated into progressively larger structures, ultimately forming a spherulite with a radial, starburst-like morphology. This self-organization across multiple scales, from nanofibers to macroscopic crystals, is a hallmark of the far-from-equilibrium conditions maintained in the reaction–diffusion system.[39] The continuous supply of Cu^{2+}, combined with anisotropic forces, ensures that the spherulite grows symmetrically and retains its distinctive hierarchical architecture. Thus, RDF not only promotes radial growth but also fosters the creation of well-ordered, complex structures that are characteristic of spherulites. This described mechanism is clearly illustrated in the SEM micrographs where the CuAsp nanofibers are densely aggregated around the spherulite's nucleus (Fig. 2b(i–iii)). Interestingly, although the overall size of the spherulites increased (from 0.3 to 1.2 mm; Fig. 2a), the diameters of the nanofibers progressively decreased along the reaction tube (Fig. 2b(iv–vi)), ranging from 100 nm near the interface to 50 nm near the diffusion front, aligning closely with homochiral CuAsp nanofibers reported by Imaz *et al.*[9] This decrease in fiber thickness can also be attributed to the reduction of supersaturation along the tube. For example, as nucleation near the gel interface is abundant, the supply of ions is divided among many forming nuclei. This allows the nanofibers to grow thicker due to the abundance of material at the initial stages of fiber formation. This fact is reversed further away from the interface.

Noteworthy differences in precipitation Liesegang patterns were observed when comparing homochiral L-CuAsp or D-CuAsp to DL-CuAsp. Homochiral CuAsp spherulites formed densely packed arrays, while DL-CuAsp spherulites were more sparsely distributed. Liesegang bands result from periodic precipitation in reaction–diffusion systems as the reactant concentration fluctuates due to diffusion and supersaturation cycles.[38] The spacing of these bands is directly influenced by the nucleation rate, which in turn is affected by the solubility of the precipitating compound. For homochiral CuAsp, the lower solubility of L- or D-Asp (between 4 mg mL^{-1} and 5 mg mL^{-1} at 25 °C)[40,41] means that precipitation occurs more readily, leading to closely spaced Liesegang bands because the system reaches the necessary concentration for nucleation frequently along the diffusion front. This rapid

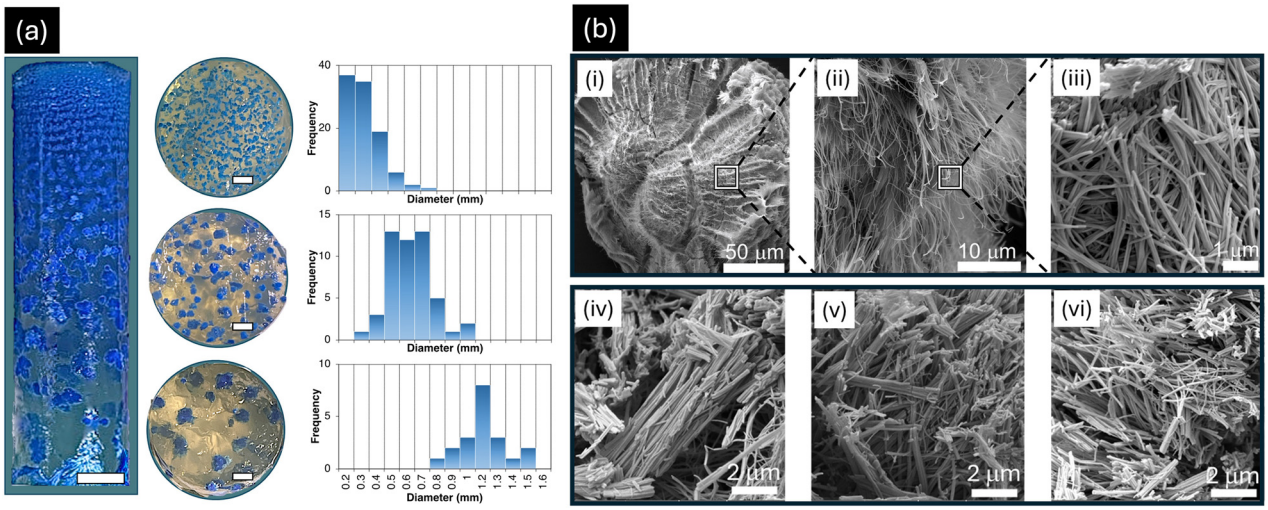

Fig. 2 (a) Periodic precipitation and particle size distribution of D-CuAsp spherulites in a 1D agar gel system (scale = 6 mm). Representative cross-sectional slices (scale = 2 mm) of the gel column highlight three distinct zones formed due to the reaction–diffusion process: The liquid–gel interface, middle zone, and bottom zone, which exhibit progressively larger spherulites, as shown in the accompanying flowchart the diameters of 100 spherulites were measured from the slice taken near the interface, 50 spherulites from the middle slice of the gel, and 20 from the lower slice of the gel. Near the liquid–gel interface, the spherulites are the smallest, with a diameter range of 0.35 ± 0.11 mm, due to the high supersaturation of Cu^{2+} ions, which promotes rapid nucleation. This leads to the formation of a large number of small crystals competing for ions. In the middle zone, where supersaturation is moderate, the spherulites reach an intermediate diameter range of 0.57 ± 0.11 mm, as nucleation slows down and crystal growth becomes more dominant. Fewer nucleation events occur in the bottom zone, with the lowest supersaturation, allowing existing crystals to grow to their largest size, with a diameter range of 1.15 ± 0.25 mm. The flowchart illustrates the size distribution across the three zones, clearly demonstrating the progression of spherulite growth as supersaturation decreases with distance from the liquid–gel interface. (b) Scanning electron microscopy (SEM) images of a D-CuAsp spherulite cross-section from the reaction tube. Panels (i–iii) show densely packed nanofibers that make up the spherulite at various magnifications. Panels (iv–vi) depict the progressive reduction in nanofiber diameters along the reaction tube, with 100 nm near the liquid–gel interface (iv), decreasing to 50 nm near the diffusion front (vi). This nanofiber size reduction correlates with the changing supersaturation levels, as larger nanofibers are observed in regions where nucleation rates are higher (closer to the interface). Initial concentrations of the outer electrolyte: [Cu^{2+}] = 300 mM; inner electrolyte: [agar] = 1%, [D-Asp] = 50 mM, [NaOH] = 100 mM; at *ca.* 22 °C.

nucleation results in shorter intervals between precipitation bands as new crystals form in quick succession. For DL-CuAsp, its higher solubility (7.8 mg mL^{-1} at 25 °C),[40,41] means that the system requires a greater concentration of Cu^{2+} ions to reach supersaturation, leading to wider spacing between precipitation events. This results in more sparsely distributed Liesegang bands, as nucleation happens less frequently due to the slower approach to supersaturation in the higher-solubility DL-Asp solution. Additionally, the slower formation of coordination complexes in DL-CuAsp, compared to homochiral CuAsp, can be attributed to the incompatibility between L- and D-Asp in nanofiber formation. This suggests that CuAsp crystallizes as a conglomerate (*vide infra*). Wu *et al.* demonstrated that mixing equal concentrations of Cu^{2+} solution with deprotonated L- or D-Asp leads to rapid gelation, while DL-Asp forms a blue gel more slowly at the same concentration, indicating faster assembly rates for homochiral CuAsp than for DL-CuAsp.[9,10]

Powder X-ray diffraction (PXRD) analysis confirmed the crystalline nature of CuAsp (Fig. 3a). Both L- and D-CuAsp exhibit the same diffraction patterns, in agreement with Wu *et al.*,[10] indicating that both forms share the same crystal packing. Remarkably, DL-CuAsp gave the same diffraction pattern. The identical PXRD patterns observed for all three forms (L-, D-, and DL-CuAsp) imply that the coordination environment around Cu^{2+} and the packing arrangement remain consistent regardless of whether the system is homochiral or racemic. This uniformity suggests that the presence of both L-and D- in DL-CuAsp does not disrupt the crystal structure but rather crystallizes in a conglomerate. Unfortunately, a detailed analysis of the structural connectivity was not feasible due to their sub-200 nm diameter nanofibers, the inability to obtain large single crystals, and the unsuccessful attempts at electron diffraction. Pawley refinement of the PXRD pattern for L-CuAsp was performed to confirm the structural integrity and phase purity of the coordination polymer. The refinement (Fig. S4†) showed excellent agreement between experimental and fitted profiles, yielding low residuals (R_{wp} = 3.87%, R_p = 2.87%). The extracted unit cell parameters (a = 22.07 Å, b = 9.17 Å, c = 5.10 Å, β = 133.95°) match the expected monoclinic symmetry (space group $P121$), and the refined crystallite size (C = 13.56 ± 0.28 nm) confirms the nanocrystalline nature of the material. These results strongly support the high crystallinity and single-phase character of the synthesized L-CuAsp. Imaz and coworkers suggested that the CuAsp nanofibers were aligned in 1D $[Cu(Asp)(H_2O)_x]_n$ polymeric chains,[9] while Wu *et al.* later proposed that the CuAsp coordination complex adopts a square-planar geometry, where the Cu^{2+} ion is bonded to the α-carboxylate

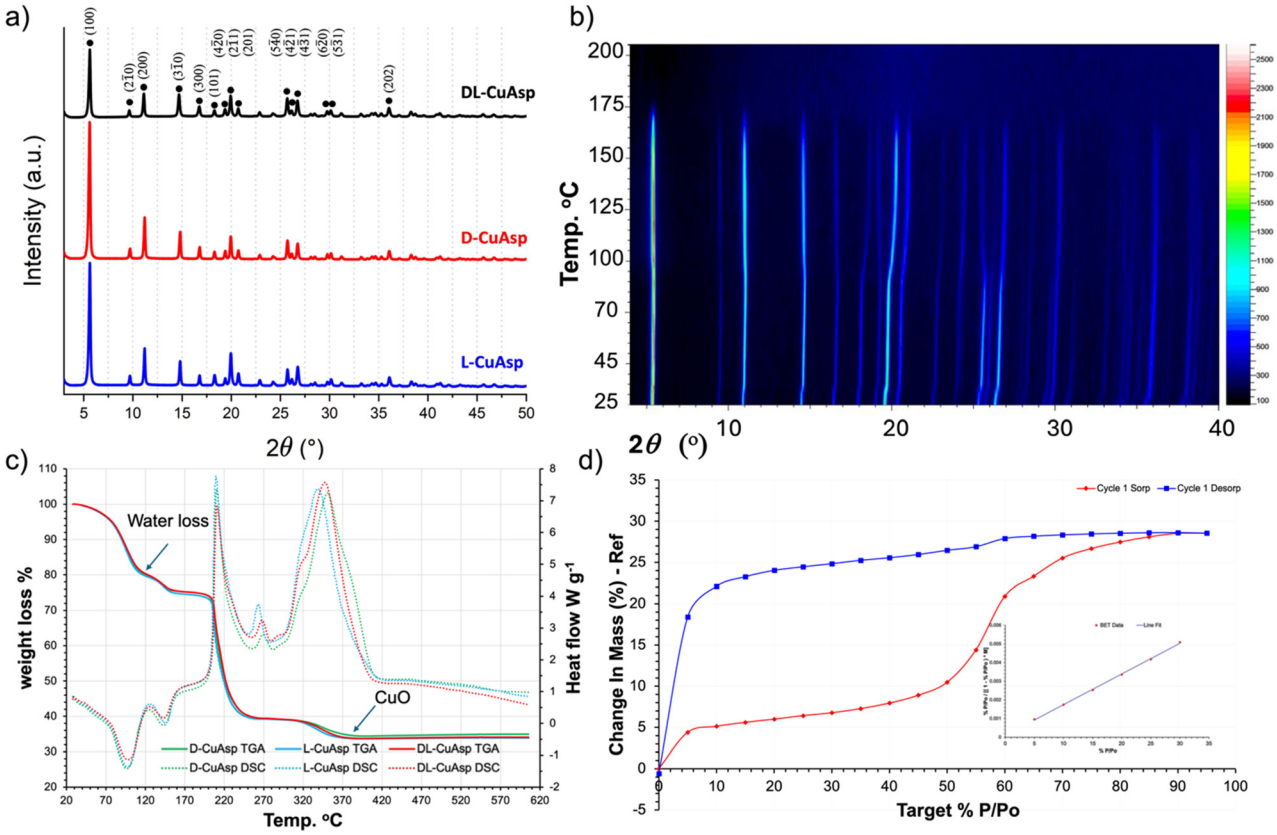

Fig. 3 Structural and thermal characterization of L-, D-, and DL-CuAsp coordination polymers. (a) PXRD patterns of L-, D-, and DL-CuAsp, showing identical diffraction profiles, confirming that DL-CuAsp crystallizes as a conglomerate. (b) Variable-temperature PXRD (VTPXRD) of L-CuAsp from 25–200 °C, showing structural integrity up to 170 °C, after which amorphization occurs. (c) TGA and DSC thermograms for L-, D-, and DL-CuAsp, showing water loss (24.7–25.2%) and final residue formation (33.8–34.8%), consistent with CuO formation at ~370 °C. (d) Dynamic vapor sorption (DVS) analysis of L-CuAsp, confirming a water uptake of 28.5%, aligning with TGA results. BET surface area (SA) calculations in the 5–30% RH range yield 170.5 $m^2\ g^{-1}$.

oxygen and amino nitrogen atoms of Asp, forming a typical five-membered glycinate chelate ring.[10]

Attenuated total reflectance Fourier-transform infrared (ATR-FTIR) characterization was performed to probe the assembly process of the nanofibers. The coordination of aspartate with Cu^{2+} is evident when comparing the IR spectra of the starting material (L-aspartic acid) with the coordination polymers L-, D-, and DL-CuAsp (Fig. S2†). A detailed analysis of the IR spectrum of L-aspartic acid reveals characteristic peaks at 3132 cm^{-1} (νN–H), 3000 cm^{-1} (νC–H), 1680 cm^{-1} (νC═O), 1612 cm^{-1} (νCOOH), and 1070 cm^{-1} (νC–N). Additional peaks at 1344 cm^{-1} and 1210 cm^{-1} correspond to C–H stretching and CH_2 twisting, respectively. Peaks at 890 cm^{-1}, 640 cm^{-1}, and 475 cm^{-1} are attributed to C–C stretching, COOH bending, and NH_3 torsion vibrations, respectively. Deprotonation of the COOH groups, prior to coordination with Cu^{2+}, is confirmed by the shift of the C═O stretching vibration to 1580 cm^{-1}.[10] The band observed at 675 cm^{-1} is attributed to Cu–O stretching, while the band at 420 cm^{-1} in all three coordination polymers corresponds to the asymmetric stretching mode of the Cu–N bonds (395–455 cm^{-1}).[42,43] All three CPs, L-, D-, and DL-CuAsp CPs, exhibit virtually identical IR spectra.

We conducted further experiments to shed light on the underlying CuAsp structure. The IR shows a broad peak in the range of 2800–3600 cm^{-1}, corresponding to the presence of water molecules. To confirm the presence of water as part of the structure, the thermal stability of the compound L-CuAsp was investigated using variable temperature PXRD (VTPXRD) and thermogravimetric analysis (TGA). The VTPXRD reveals changes in 2θ, especially at 18.1°, 19.2°, 19.5°, 25.4°, and 26.2°, starting when the sample was heated from 90 °C until 125 °C. These changes may correspond to the loss of solvents from the structure. The temperature and experimental preparation suggest the loss of free water molecules at around 90 °C, while the coordinated water molecules can be released above 110 °C (Fig. 3b). The structure remains intact up to 170 °C, followed by the material's complete amorphization. TGA was used to investigate the number of water molecules in the structure (Fig. 3c). The weight loss due to water ends at 130 °C, with a weight loss drop of approximately 27%. The material then shows thermal stability between 170–200 °C, which aligns very well with the amorphization of the compound, as observed in the VTPXRD. The decomposition led to the formation of CuO at 370 °C. Interestingly, the calculated

number of water molecules from the weight loss is approximately four. It is worth mentioning that the pure enantiomers and the racemate have the same profile and weight loss, indicating they have a similar structure, which agrees with conglomerate crystallization and supports the results from the PXRD analysis. The water uptake of a dry sample of L-CuAsp was also investigated using dynamic vapour sorption (DVS, Fig. 3d). First, the CP was activated by heating the sample at 100 °C for 4 hours; then, the dried sample was placed on the DVS, and the relative humidity was gradually increased starting from 0 RH% up to 95 RH%, with increments of 5 RH%. The compound shows a water uptake and desorption of 28.5%, which agrees with the TGA results. Based on the DVS results, the surface area (SA) calculation using the Brunauer–Emmett–Teller (BET) method shows an SA of 170.5 $m^2\ g^{-1}$.

To assess porosity, N_2 adsorption–desorption isotherms of L-, D-, and DL-CuAsp were measured at 77 K (Fig. S3†), all exhibiting type IV isotherms with H3-type hysteresis loops. These features indicate mesoporosity and are typically associated with slit-like pores formed by fibrous aggregates. While PXRD confirms that the L-, D-, and DL-CuAsp coordination polymers share the same crystalline phase, nitrogen sorption measurements reveal differences in their textural properties. DL-CuAsp exhibits the largest total pore volume (0.684 $cm^3\ g^{-1}$), the highest average BET pore diameter (293.6 Å), and a BET surface area of 93.2 $m^2\ g^{-1}$—indicative of substantial mesoporosity, likely due to looser crystallite packing or interparticle voids formed by mixing of L- and D-domains. In contrast, the enantiopure forms show comparable BET surface areas—88.1 $m^2\ g^{-1}$ for L-CuAsp and 93.7 $m^2\ g^{-1}$ for D-CuAsp—but smaller average pore diameters (76.6 Å for L-CuAsp and 39.7 Å for D-CuAsp) and lower total pore volumes (0.169 $cm^3\ g^{-1}$ and 0.093 $cm^3\ g^{-1}$, respectively). The initial rapid uptake at low relative pressures corresponds to monolayer formation in mesopores, while the steep uptake at higher pressures is attributed to capillary condensation. The observed hysteresis further supports the presence of non-rigid, fibrous pore architectures.[44] Micropore surface areas and volumes also differ (L-CuAsp: 26.6 $m^2\ g^{-1}$, 0.0111 $cm^3\ g^{-1}$; D-CuAsp: 84.8 $m^2\ g^{-1}$, 0.0327 $cm^3\ g^{-1}$), but these variations are likely due to sample preparation or measurement variability, as the materials are mirror-image isostructures. Thus, deviations in BET parameters are interpreted as experimental scatter rather than inherent differences in porosity.

Solid-state circular dichroism (CD) was employed to investigate the chirality of CuAsp polymers (Fig. 4). L-CuAsp exhibited a positive Cotton effect, while D-CuAsp showed a negative Cotton effect at 745 nm, with both crossing at 655 nm, indicating the presence of a chiral coordination sphere of the Cu^{2+} with chiral Asp.[9] In contrast, DL-CuAsp showed no Cotton effect, nor did the individual DL-CuAsp spherulites (Fig. S5†). This observation apparently contradicts crystallization as a conglomerate, as indicated by the identical PXRD pattern shared by DL- and homochiral CuAsp.

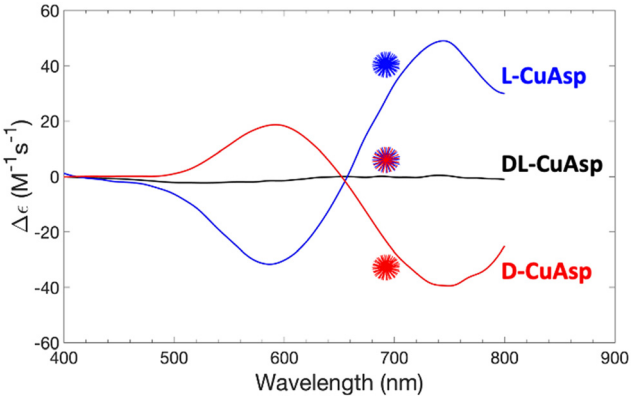

Fig. 4 Solid-state circular dichroism (CD) spectra of L-CuAsp (blue), D-CuAsp (red), and DL-CuAsp (black), demonstrating their chiral properties. L-CuAsp exhibits a positive Cotton effect, while D-CuAsp shows a negative Cotton effect at 745 nm, both crossing at 655 nm, confirming their enantiomeric nature. In contrast, DL-CuAsp shows no Cotton effect, indicating the absence of net chirality. The results suggest that while individual nanofibers within DL-CuAsp spherulites remain homochiral, their racemic aggregation cancels out the overall chiral signal. These findings confirm that CuAsp crystallizes as a conglomerate, as further supported by PXRD analysis.

Herein, it is believed that the nanofibers within each DL-CuAsp spherulite are individually homochiral. Still, their aggregation presents racemic-like behavior in CD analysis, reconciling the PXRD data with the lack of chiral signals in the CD results. These findings demonstrate that RDF enables the periodic precipitation of L-, D-, and DL-CuAsp coordination polymers in agar gel.

Chiral resolution of DL-Asp in the presence of homochiral proline (Pro)-copper complexes in agar gel

Homochiral L- and D-Pro-copper complexes as tailor-made additives (TMAs) were used to achieve spatiotemporal chiral resolution of DL-Asp in the gel. The diffusion of homochiral Pro-copper complexes (L-Pro or D-Pro) into the agar gel containing DL-Asp results in spatially distinct bands of CuAsp coordination polymers. The spatial organization is guided by the concentration gradients established by RDF, which controls where and how the chiral molecules crystallize. Drawing from Harada's research, when the mole ratio of the chiral amino acid to DL-Asp is less than 1, the second crop of crystals maintains the same configuration as the first crop. Yet, when the mole ratio is equal to or greater than 1, the configuration of the second crop reverses relative to the first crop.[27] To confirm proper complexation, UV-vis absorption analysis was performed, revealing an adsorption shift from 800 nm to approximately 725 nm regardless of the concentration of Pro, indicating the formation of a Pro-Cu(II) complex in solution (Fig. S6†).

After diffusing chiral Pro-copper complexes into DL-Asp gel, distinct spatiotemporal regions of CuAsp polymers were observed (Fig. 5). The evolution of this periodic precipitation is shown in Fig. S7.† Samples obtained near the interface

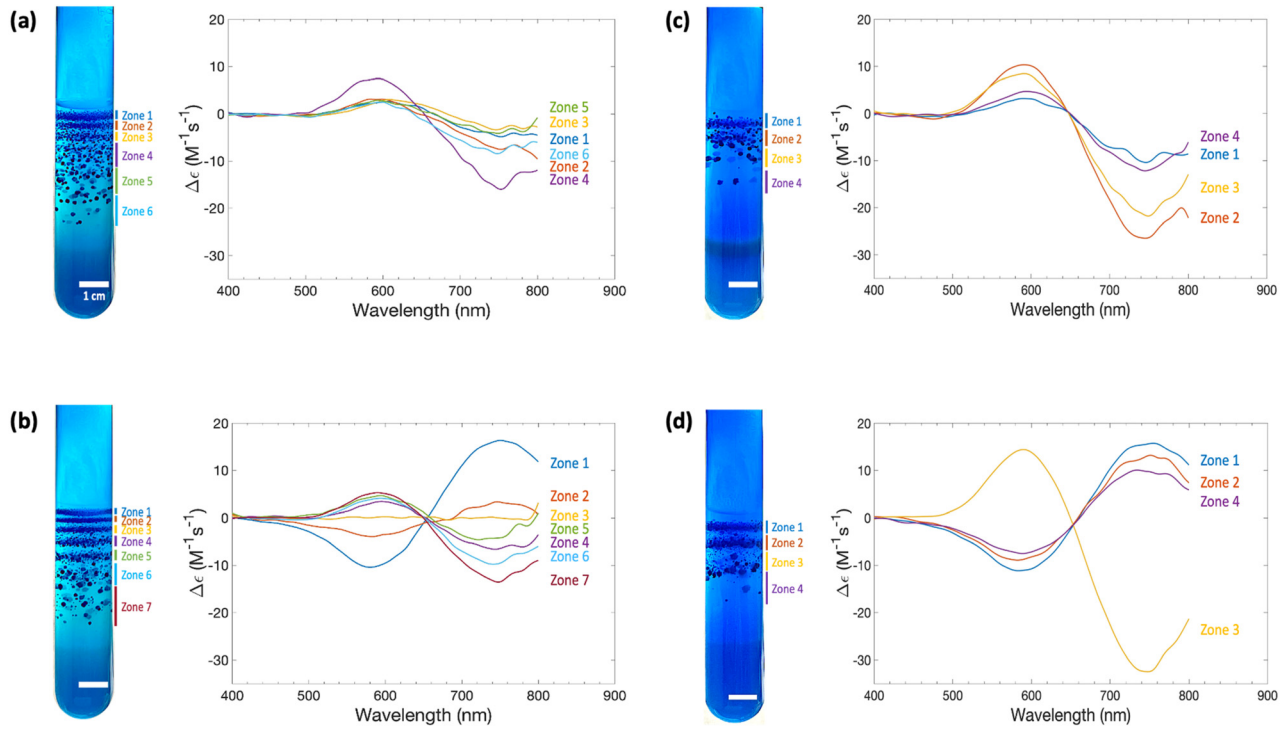

Fig. 5 Crystallization of DL-CuAsp coordination polymers in a 1% agar gel in the presence of homochiral proline-copper (Pro-Cu) complexes, illustrating the effect of different concentrations on chiral resolution. (a) and (b) show crystallization in the presence of 100 mM L-Pro-Cu and 100 mM D-Pro-Cu complexes, respectively, while (c) and (d) correspond to crystallization with 200 mM L-Pro-Cu and 200 mM D-Pro-Cu complexes. The spatial distribution of CuAsp precipitates was analyzed using solid-state circular dichroism (CD) spectroscopy, with spectra shown for each precipitate zone. For all experiments, the inner electrolyte contained 50 mM DL-Asp, and 100 mM NaOH in 1% agar. The outer electrolyte for (a) and (b) consisted of 300 mM Cu^{2+}, 100 mM Pro, and 100 mM NaOH, while for (c) and (d), it contained 300 mM Cu^{2+}, 200 mM Pro, and 200 mM NaOH. Experiments were conducted at ~22 °C.

consistently showed chirality opposite to the introduced TMAs. Solid-state CD analysis reveals a negative Cotton effect in the presence of L-Pro-copper complexes, suggesting the predominance of D-CuAsp (Fig. 5a and c). In contrast, the presence of D-Pro-copper complexes led to positive Cotton effects, indicating L-CuAsp formation near the liquid–gel interface (Fig. 5b and d). These findings align with the 'rule of reversal', where the presence of a homochiral additive influences the chiral environment, promoting the crystallization of the opposite enantiomer. However, the overall chiral intensity decreased when L- and D-Pro-copper complexes were introduced, compared to the coordination polymers formed in the absence of TMAs. This suggests that although these TMAs selectively attached to the nanofibers of the conglomerates with the same configuration, they only partially resolved the DL-Asp conglomerates. This differential impact could be attributed to the inherent differences in how L- and D-Pro complexes interact with DL-Asp and the agar gel environment. Notably, fewer precipitates formed at higher concentrations of Pro-copper complexes than those formed at lower concentrations, likely due to the slower coordination rate: at higher concentrations, the Pro-copper complexes may create a denser environment around the aspartate ligands, leading to increased steric hindrance and reduced mobility. This congestion can slow the rate at which the Pro-copper complexes effectively coordinate with the aspartate, impeding efficient nucleation and subsequent crystal growth. The slower coordination rate thus limits the number of nucleation sites available, resulting in a reduced number of precipitates despite the higher concentration of reactants. Additionally, higher concentrations of TMAs may promote the formation of transient or less stable intermediates, further delaying or hindering the crystallization process.

During crystallizations involving L-Pro-copper additive, mainly coordination polymers with negative Cotton effects were observed across all zones (Fig. 5a and c), indicating the predominant formation of D-CuAsp. A lower chiral intensity was observed with 100 mM L-Pro-copper than 200 mM L-Pro-copper. In the case of 100 mM D-Pro-copper additive, a gradual chiral switching of the coordination polymers from positive to negative Cotton effect was observed (Fig. 5b). In contrast, two chiral switching events occurred in the presence of 200 mM D-Pro (Fig. 5d). This switching develops on Harada's work in solution and is attributed to the slower coordination rates and higher steric hindrance introduced by the excessive presence of Pro-copper complexes, which could inhibit effective nucleation and crystallization. The reduced efficiency suggests an optimal concentration range for the TMAs where they exert maximum influence on the chiral resolution process. Beyond this range, the coordination

kinetics may not favor the formation of organized chiral domains.

A factor that can rationalize the effect of L- and D-Pro-copper additive on the chiral distribution of CuAsp could be related to the composition of the agar gel itself, which primarily consists of D-galactose. In the context of the 'rule of reversal', the gel may also influence the chiral crystallization of CuAsp.[29] In other words, the agar could act as a chiral competitor, diminishing the chiral influence of the D-Pro-copper additive. This would be particularly noticeable as the distance from the interface increases and the concentration of the TMA decreases, allowing the agar's intrinsic chirality to become more influential. This result may indicate that while the RDF can create favorable conditions for chiral resolution, the specific chiral interactions and competition with the gel matrix must be considered to optimize the outcome.

Theoretical model

To provide a quantitative understanding of the observed spatiotemporal chiral resolution in RDF, we developed a theoretical model coupling classical reaction–diffusion equations with Cahn–Hilliard equations to describe Liesegang precipitate formation and evolution for the L- and D-enantiomers of CuAsp in the presence of homochiral copper-proline complexes as tailor-made additives (TMAs). Notably, the Cahn–Hilliard equations inherently account for phase separation driven by the competition between diffusion and phase segregation, effectively mimicking the periodic banding observed in Liesegang patterns. This characteristic arises from the interplay between local supersaturation, nucleation kinetics, and diffusive transport, generating alternating regions of precipitate-rich and precipitate-poor phases.[45–47]

The general formulation of the model includes concentration fields for the Cu^{2+} ions (C), L- and D-aspartate ions (A_L, A_D), and L-Pro-copper complexes (P_L). The precipitates formed by the coordination polymers of L- and D-CuAsp are represented by volume fractions ϕ_L and ϕ_D, respectively. The dynamics of the system are governed by reaction–diffusion equations coupled to the phase separation described by the Cahn–Hilliard equations.

The reaction–diffusion equations of all components are given by:

$$\frac{\partial C}{\partial t} = D_C \nabla^2 C - R_L - R_D \quad (1)$$

$$\frac{\partial A_L}{\partial t} = D_A \nabla^2 A_L - R_L - R_{PL} \quad (2)$$

$$\frac{\partial A_D}{\partial t} = D_A \nabla^2 A_D - R_D - R_{PD} \quad (3)$$

$$\frac{\partial P_L}{\partial t} = D_P \nabla^2 P_L - R_P - R_{PL} - R_{PD} \quad (4)$$

where D_C, D_A, and D_P represent the diffusion coefficients for Cu^{2+} ions, Asp ions, and Pro-copper complexes, respectively; the reaction terms are explicitly written as:

$$R_L = k_L \times C \times A_L;\ R_D = k_D \times C \times A_D \quad (5)$$

$$R_{PL} = k_{PL} \times P_L \times A_L;\ R_{PD} = k_{PD} \times P_L \times A_D \quad (6)$$

The reaction rates R_L and R_D represent the polymerization rates of L- and D-CuAsp formed *via* the direct reaction between free copper ions and aspartate. Since this process does not involve any chiral influence, the rate constants k_L and k_D are expected to be equal, reflecting the intrinsic symmetry of the racemic system in the absence of a chiral selector. In contrast, R_{PL} and R_{PD} describe the polymerization rates arising from the interaction between the L-proline-copper complex, for example, and aspartate. Here, the chiral environment introduced by the L-proline ligand is expected to differentiate between L- and D-aspartate, leading to distinct rate constants k_{PL} and k_{PD}. These rate constants, representing stereoselective ligand exchange, are hypothesized to differ in magnitude, and this asymmetry is proposed to be a factor governing the enantiomeric bias observed in the resulting Liesegang bands. Furthermore, when L-proline is replaced with its mirror image, D-proline, the stereochemical preference is reversed, causing the relative magnitudes of k_{PL} and k_{PD} to switch accordingly. This reversal underscores the chiral origin of the selectivity in the reaction pathway.

The Cahn–Hillard equations that describe the time evolution of the order parameters (precipitate volume fractions) representing the coordination polymers, ϕ_L and ϕ_D, are given by:

$$\frac{\partial \phi_L}{\partial t} = M_L \nabla^2 \left[-\gamma_L \nabla^2 \phi_L + \frac{\delta f}{\delta \phi_L} \right] + R_L + R_{PL} \quad (7)$$

$$\frac{\partial \phi_D}{\partial t} = M_D \nabla^2 \left[-\gamma_D \nabla^2 \phi_D + \frac{\delta f}{\delta \phi_D} \right] + R_D + R_{PD} \quad (8)$$

where M_L and M_D are the mobilities of the precipitates, assumed to be constants; γ_L and γ_D controls the interfacial energies.

To account for the asymmetric behavior observed between the L- and D-coordination polymers, we consider a generalized free energy density $f\phi_L$, ϕ_D that includes distinct thermodynamic parameters for each enantiomer and assumes a double-well potential function:

$$f(\phi_L, \phi_D) = \sum_{i=L,D} \left(-\frac{a_i}{2} \phi_i^2 + \frac{b_i}{4} \phi_i^4 \right) + \chi \phi_L \phi_D \quad (9)$$

Specifically, the nucleation barrier and phase stability of the L- and D-precipitates are governed by the parameters a_L, b_L, a_D, b_D, respectively. The quadratic coefficients a_L and a_D control the ease of nucleation for each precipitate, with larger values corresponding to lower nucleation barriers. The quartic coefficients b_L and b_D determine the thermodynamic

stability and saturation levels of the respective precipitated phases, effectively capturing differences in solubility between the L- and D-complexes. The coupling term $\chi\phi_L\phi_D$ explicitly controls interactions between the two enantiomeric phases; here, a positive value of α corresponds to mutual exclusion, whereas a negative value of α, as employed in our simulations, explicitly promotes coexistence and mixing between enantiomeric precipitates. Additionally, spatial gradients of the order parameters in eqn (8) and (9) are penalized through interfacial energy terms, explicitly controlling the width and sharpness of the Liesegang bands. This generalized framework enables us to capture the experimentally observed differences in kinetic and thermodynamic behavior between racemic and chiral conditions.

Numerical solutions and results

The Cahn–Hilliard eqn (7) and (8)—used to capture phase separation and band formation—are solved in tandem with the RD eqn (1)–(4) to account for simultaneous diffusion, nucleation, and precipitate growth. By adjusting the nucleation barrier (a), stability (b), and enantiomeric coupling (χ) parameters, the simulations reproduce both the classical Liesegang spacing/width laws and the chiral inversion phenomena observed experimentally.

The spatial domain is discretized using a second-order finite difference scheme for all Laplacian terms, applying Dirichlet or Neumann boundary conditions as appropriate (*e.g.*, Dirichlet for concentration at the gel inlet, no-flux for the precipitates). We employ the method of lines, converting the PDE system into a large set of ordinary differential equations (ODEs) for each grid point. A stiff ODE solver (such as MATLAB's ODE15s) then integrates these ODEs in time, ensuring stability under the often-steep gradients characteristic of Liesegang precipitation.

Fig. 6(a) presents numerical simulation results obtained in the absence of any chiral proline additive. Initially, the gel contains equal concentrations of L- and D-aspartate enantiomers, representing a racemic mixture, with copper ions introduced as an inner electrolyte diffusing into the gel. The parameters used in this simulation were set symmetrically for both enantiomers ($a_L = a_D = 0.5$, $b_L = b_D = 0.5$) to ensure equivalent nucleation barriers and equilibrium stability. Additionally, a small negative coupling constant (χ) = −0.01 was chosen, explicitly promoting the coexistence of both enantiomeric precipitates. Under these conditions, clear and well-defined Liesegang bands formed for both normalized ϕ_L and ϕ_D, demonstrating periodic precipitation along the spatial domain. Notably, the resulting band pattern follows classical Liesegang laws: the spacing between consecutive bands increases with distance from the gel–electrolyte interface (spacing law), and the band widths also increase progressively along the same direction (width law). The solutions for ϕ_L and ϕ_D overlap strongly in both position and amplitude, confirming the formation of a racemic

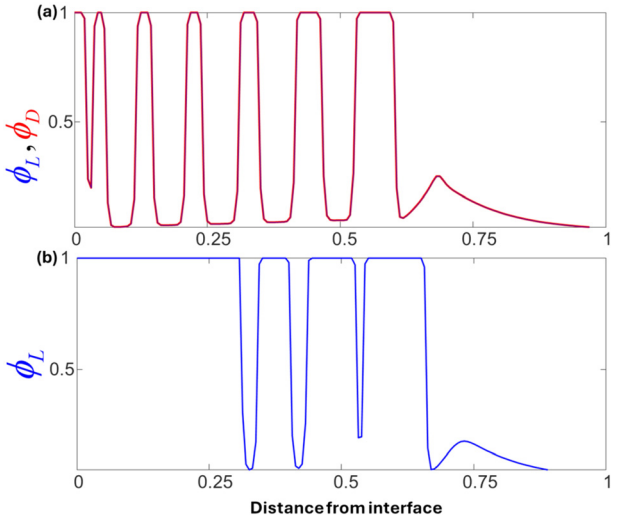

Fig. 6 Simulated Liesegang banding profiles for enantiomeric coordination polymers. (a) Racemic case: The gel initially contains equal concentrations of L- and D-aspartate ($A_L = A_D = 0.5$), with copper ions introduced from the left boundary ($C_0 = 2$). Symmetric parameters were used for both enantiomers: $a_L = a_D = 0.5$, $b_L = b_D = 0.5$, and coupling constant $\chi = -0.01$. Clear and overlapping bands are observed for ϕ_L and ϕ_D, consistent with the formation of an achiral (racemic) coordination polymer. The band structure follows classical Liesegang spacing and width laws. (b) Chiral case: The gel contains only L-aspartate ($A_L = 1$), at the same total concentration as in the racemic case. To reflect the increased solubility and reduced stability of the enantiopure system, the parameters were set to $a_L = 0.55$, $b_L = 0.45$, and $\chi = 0$. The resulting pattern shows fewer Liesegang bands, with the initial region dominated by a continuous precipitation zone, in agreement with experimentally observed differences under chiral conditions. In both cases, the interfacial penalty $\gamma = 0.1$, the mobility $M = 0.05$, and the diffusivity of copper and aspartate $D_C = 1$, $D_A = 0.6$, respectively. The distance from the interface is scaled with respect to the length of the reactor.

(achiral) coordination polymer. This result aligns closely with experimental observations, reinforcing that racemic starting conditions yield exclusively achiral Liesegang band structures. Fig. 6(b) shows the results of a simulation in which only L-aspartate is initially present in the gel, at the same concentration as the total aspartate content in the racemic case of Fig. 6a. This setup mimics enantiopure conditions without any chiral additive. To reflect the known increase in solubility and reduced stability of enantiopure coordination polymers compared to racemic ones, we selected a higher nucleation barrier ($a_L > 0.5$) and a lower stability parameter ($b_L < 0.5$) than those used in Fig. 1a. These parameter choices explicitly encode the experimentally observed solubility differences and account for the altered precipitation behavior of the pure enantiomer system. The resulting Liesegang pattern is markedly different from the racemic case: while banding still emerges, the number of discrete bands is reduced, and they appear further from the source of copper diffusion. Moreover, the early region near the gel–electrolyte interface is dominated by a continuous precipitation zone rather than distinct bands. This qualitative change in pattern morphology is consistent with

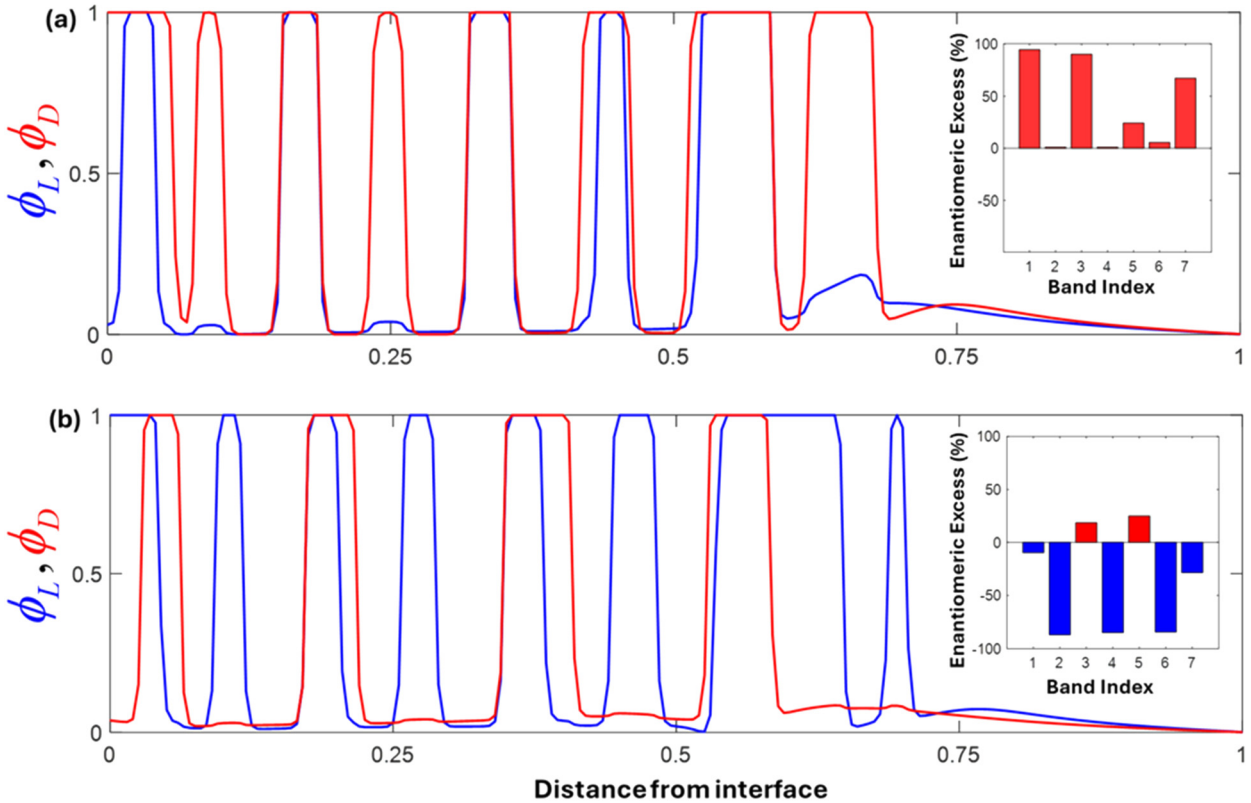

Fig. 7 Numerical simulations of Liesegang band formation in the presence of chiral dopants. (a) L-Proline additive: The upper panel shows the resulting precipitate distributions for D-aspartate (red) and L-aspartate (blue) when the system is doped with L-proline. The parameters are chosen such that $a_D < a_L$ and $b_D > b_L$ (a_D = 0.4, a_L = 0.6; b_D = 0.6, b_L = 0.4) reflecting the lower nucleation barrier and higher stability of the D-enantiomer. Consequently, the D-precipitate forms prominently in the early and subsequent bands, with L-precipitate remaining suppressed until the far end of the domain. The exchange rate constants k_{PL} = 0.1 and k_{PD} = 0.05. The inset bar chart shows the enantiomeric excess (EE) per indexed band, demonstrating strong D-dominance (positive EE) in the earliest bands, consistent with the phenomenon of chiral inversion reported in this work (b) D-proline additive: The lower panel illustrates the case in which the system is doped with D-proline. Here, $a_L < a_D$ and $b_L > b_D$ (a_D = 0.6, a_L = 0.4; b_D = 0.4, b_L = 0.6) favor the L-precipitate (blue) in the early Liesegang bands. As the reaction–diffusion front advances, however, band-by-band 'switching' in the enantiomeric excess occurs, evidenced by the inset bar chart showing an EE that alternates between L-enriched and D-enriched. This switching behavior highlights the interplay of doping, diffusion, and nucleation processes, capturing the experimentally observed transitions in handedness during chiral resolution. Both panels underscore the ability of tuned *aa* and *bb* parameters to reproduce known experimental outcomes in chiral Liesegang banding. The exchange rate constants k_{PL} = 0.05 and k_{PD} = 0.1. In both cases, initial copper, copper proline complex, and aspartate C_0 = 1, C_{P0} = 2 and $A_{L,D}$ = 0.5, the interfacial penalties $\gamma_{L,D}$ = 0.1, the mobilities $M_{L,D}$ = 0.05, and the diffusivity of copper, copper proline complex, and aspartate D_C = 1, D_P = 0.9, D_A = 0.6, respectively.

experimental reports of altered Liesegang structures under enantiopure conditions, and it highlights the model's capacity to capture the subtle interplay between solubility, nucleation kinetics, and pattern formation in chiral systems.

Fig. 7(a) presents the simulated Liesegang bands in the presence of L-proline as a chiral additive. To reflect the experimental observation that early bands precipitate with the opposite chirality to the additive (Harada *et al.*), we selected parameters such that the D-coordination polymer has a lower nucleation barrier and higher stability ($a_L > a_D$, $b_L < b_D$), making D-aspartate more likely to nucleate and grow initially. Consistent with Harada's results, the plot shows that the D-precipitate (red) dominates in both early and subsequent bands, while the L-precipitate (blue) remains suppressed until late in the gel. The inset bar chart quantifies the enantiomeric excess (EE) for each indexed band, demonstrating a strongly positive (D-favored) EE in the earliest bands, which gradually evolves but remains predominantly D-enriched. This matches the "chirality inversion" phenomenon in which the enantiomeric configuration of the precipitate is opposite to that of the additive in initial Liesegang bands.

In contrast, Fig. 7(b) illustrates the scenario when D-proline is used. Here, we reverse the parameter assignments such that L-aspartate (blue) is initially favored (lower a_L, higher b_L), reflecting the reported inversion in which the precipitate's handedness initially opposes that of the dopant. Indeed, the early bands now predominantly show an L-configuration (blue). Over time, however, the enantiomeric excess switches from L-negative to D-positive and back again, as shown in the inset bar plot where some bands exhibit strong L-enrichment while others flip to D-dominance. Such a switching phenomenon has also been observed experimentally in chiral resolution systems,

pointing to subtle kinetic–thermodynamic interactions in the presence of a strong chiral dopant. This highlights that as the reaction–diffusion front moves, and local conditions (*e.g.*, concentration of free proline) change, the favored enantiomer can shift accordingly. It is also noteworthy that it was ultimately found that the asymmetry in the kinetic parameters *a* and *b* plays a more dominant role than the ligand exchange rate constants themselves in determining the extent of enantiomeric excess in the banding pattern.

Overall, these simulations align well with the key findings in this work, which showed that adding L- or D-proline to racemic aspartic acid solutions can yield initial precipitates of the opposite chirality, and that later bands can partially switch or evolve in handedness. The adjustments to the nucleation barrier (*a*) and stability (*b*) for each enantiomeric species (L *vs.* D) successfully capture these effects: the aspartate with the lower effective *aa* and higher *bb* spontaneously nucleates earlier, forming the earliest Liesegang bands, while the other enantiomer may eventually precipitate in later bands or intersperse periodically, leading to the observed "flip" or switching behavior in enantiomeric excess.

Conclusions

In this study, we demonstrated a reaction–diffusion framework (RDF) that drives both the formation and chiral resolution of CuAsp coordination polymers. Experimentally, homochiral L- or D-aspartate formed dense Liesegang bands, while racemic DL-aspartate produced more widely spaced bands, reflecting their solubility differences. Solid-state CD confirmed that DL-CuAsp behaved as a conglomerate, showing no net chiral signal despite its homochiral nanofibers. When L- or D-proline copper complexes (TMAs) were introduced to a DL-Asp gel, chiral inversion was observed at the gel interface, consistent with Harada's earlier findings. Further from the interface, local conditions (additive depletion, agar gel chirality, and changing supersaturation) promoted partial switching in enantiomeric excess, highlighting a dynamic interplay of diffusion and kinetic/thermodynamic factors.

By incorporating a newly added theoretical and numerical simulation section, we showed how modified reaction–diffusion and Cahn–Hilliard equations comprehensively reproduce these experimental behaviors. We set distinct nucleation (*a*) and stability (*b*) parameters in line with Harada's solubility-based rationale, accurately capturing racemic *versus* enantiopure scenarios as well as TMA-induced chiral inversion and band-by-band switching. The simulations not only confirm the experimentally observed Liesegang band spacing and width laws but also illuminate how fine-tuning such parameters can yield different chiral outcomes. Overall, our results highlight the RDF's capability – complemented by predictive simulations – to enable chiral resolution *in situ* while forming well-defined coordination polymer structures. In the context of this study, both experimental and simulated results support this behavior: early Liesegang bands form with the opposite handedness to the proline dopant, while later bands show chiral switching as local conditions evolve. This dynamic phenomenon, captured through the interplay of RDF, Cahn–Hilliard modeling, and chiral TMAs, underscores the *rule of reversal* as a hallmark of nonequilibrium chiral crystallization. Future research will extend these approaches to other amino acids or ligands, exploring advanced gel matrices and dopants, thereby refining this combined experimental modeling platform for chiral material design and chiral resolution.

Data availability

The data supporting this work is included within the main article and/or the ESI.†

Author contributions

Poh Ying Fong: investigation, visualization, formal analysis, writing – original draft; Sehrish Khan: investigation, visualization, formal analysis; Hatem M. Titi: investigation, formal analysis, visualization, writing; Manal Ammar: investigation, formal analysis; Fiorenzo Vetrone: supervision, resources, conceptualization, editing; Mazen Al-Ghoul: supervision, conceptualization, investigation, methodology, theory and simulation, writing; Louis A. Cuccia: supervision, resources, funding acquisition, conceptualization, investigation, methodology, writing.

Conflicts of interest

There are no conflicts to declare.

Acknowledgements

Financial support from NSERC Canada, the FQRNT-supported multi-university Québec Centre for Advanced Materials (QCAM), and Concordia University are greatly acknowledged. MAG acknowledges the support from the American University of Beirut Research Board. Clauda Medlej is acknowledged for BET measurements. We thank Dr. Ashlee Howarth for allowing access to PXRD instrumentation and Dr. Mihails Arhangelskis for his support with the crystal structure studies.

References

1 G. Chakraborty, I.-H. Park, R. Medishetty and J. J. Vittal, *Chem. Rev.*, 2021, **121**, 3751–3891.
2 E. R. Engel and J. L. Scott, *Green Chem.*, 2020, **22**, 3693–3715.
3 J. Zhang, W. Kosaka, Y. Kitagawa and H. Miyasaka, *Nat. Chem.*, 2021, **13**, 191–199.
4 H. Li, K. Wang, Y. Sun, C. T. Lollar, J. Li and H.-C. Zhou, *Mater. Today*, 2018, **21**, 108–121.
5 L. Jiao, *Adv. Mater.*, 2018, **30**, e1703663.

6 S. Wang, Y. Hou, E. Wang, Y. Li, L. Xu, J. Peng, S. Liu and C. Hu, *New J. Chem.*, 2003, **27**, 1144–1147.
7 I. Imaz, M. Rubio-Martínez, L. García-Fernández, F. García, D. Ruiz-Molina, J. Hernando, V. Puntes and D. Maspoch, *Chem. Commun.*, 2010, **46**, 4737–4739.
8 C. Cruz, C. Gonzalez, F. Rubio, J. Erices, K. Wrighton-Araneda, D. Cortés-Arriagada, D. Venegas-Yazigi, N. Audebrand and V. Paredes-García, *Cryst. Growth Des.*, 2022, **22**, 237–250.
9 I. Imaz, M. Rubio-Martínez, W. J. Saletra, D. B. Amabilino and D. Maspoch, *J. Am. Chem. Soc.*, 2009, **131**, 18222–18223.
10 H. Wu, C. Tian, Y. Zhang, C. Yang, S. Zhang and Z. Jiang, *Chem. Commun.*, 2015, **51**, 6329–6332.
11 M. Mizutani, N. Maejima, K. Jitsukawa, H. Masuda and H. Einaga, *Inorg. Chim. Acta*, 1998, **283**, 105–110.
12 C. Wang, N. Zhang, C.-Y. Hou, X.-X. Han, C.-H. Liu, Y.-H. Xing, F.-Y. Bai and L.-X. Sun, *Transition Met. Chem.*, 2020, **45**, 423–433.
13 I. Imaz, M. Rubio-Martinez, J. An, I. Sole-Font, N. L. Rosi and D. Maspoch, *Chem. Commun.*, 2011, **47**, 7287–7302.
14 J. Puigmartí-Luis, M. Rubio-Martínez, U. Hartfelder, I. Imaz, D. Maspoch and P. S. Dittrich, *J. Am. Chem. Soc.*, 2011, **133**, 4216–4219.
15 Q. Zhou, R. Sun, Y. Ren, R. Tian, J. Yang, H. Pang, K. Huang, X. Tian, L. Xu and Y. Tang, *Carbon Energy*, 2023, **5**(1), e273.
16 C. Li, K. Deng, Z. Tang and L. Jiang, *J. Am. Chem. Soc.*, 2010, **132**, 8202.
17 F. Pu, X. Liu, B. Xu, J. Ren and X. Qu, *Chem. – Eur. J.*, 2012, **18**, 4322–4328.
18 O. Shemchuk, F. Grepioni, T. Leyssens and D. Braga, *Isr. J. Chem.*, 2021, **61**, 563–572.
19 L. Addadi, Z. Berkovitch-Yellin, N. Domb, E. Gati, M. Lahav and L. Leiserowitz, *Nature*, 1982, **296**, 21–26.
20 G. Coquerel, *Novel Optical Resolution Technologies*, 2007, pp. 1–51.
21 G. Springuel and T. Leyssens, *Cryst. Growth Des.*, 2012, **12**, 3374–3378.
22 B. Tang, W. Wang, H. Hou, Y. Liu, Z. Liu, L. Geng, L. Sun and A. Luo, *Chin. Chem. Lett.*, 2022, **33**, 898–902.
23 H. L. Lee, Y. L. Hung, A. Amin, D. E. Pratama and T. Lee, *Ind. Eng. Chem. Res.*, 2023, **62**, 1946–1957.
24 K. Harada, *Nature*, 1965, **205**, 590–591.
25 K. Harada, *Bull. Chem. Soc. Jpn.*, 1965, **38**, 1552–1555.
26 K. Harada and T. Iwasaki, *Chem. Lett.*, 1972, **1**, 1057–1059.
27 K. Harada and W. Tso, *Bull. Chem. Soc. Jpn.*, 1972, **45**, 2859–2862.
28 L. Addadi, J. van Mil, E. Gati and M. Lahav, *Amplification of optical activity by crystallization in the presence of tailor-made additives. The* "*inversion rule*", Springer, 1981, pp. 355–364.
29 J. Van Mil, L. Addadi, E. Gati and M. Lahav, *J. Am. Chem. Soc.*, 1982, **104**, 3429–3434.
30 I. Weissbuch, L. Addadi, L. Leiserowitz and M. Lahav, *J. Am. Chem. Soc.*, 1988, **110**, 561–567.
31 P. Kongsamai, C. Flood, J. H. Horst and A. E. Flood, *Chem. Eng. Technol.*, 2018, **41**, 1173–1179.
32 L. Gou, H. Lorenz and A. Seidel-Morgenstern, *Cryst. Growth Des.*, 2012, **12**, 5197–5202.
33 J. Sun, Y. Wang, Z. Gao, J. Gong and W. Tang, Additive-assisted preferential crystallization of racemic component: A case of norvaline, *J. Ind. Eng. Chem.*, 2022, **110**, 206–216.
34 E. Nakouzi and O. Steinbock, *Sci. Adv.*, 2016, **2**, e1601144.
35 R. Issa, M. Hmadeh and M. Al-Ghoul, *Trans. Tech. Publ.*, 2017, **380**, 39–47.
36 R. Issa, F. A. Ibrahim, M. Al-Ghoul and M. Hmadeh, *Nano Res.*, 2021, **14**, 423–431.
37 R. Zakhia Douaihy, M. Al-Ghoul and M. Hmadeh, *Small*, 2019, **15**, 1901605.
38 H. Nabika, M. Itatani and I. Lagzi, *Langmuir*, 2019, **36**, 481–497.
39 A. G. Shtukenberg, Y. O. Punin, E. Gunn and B. Kahr, *Chem. Rev.*, 2012, **112**, 1805–1838.
40 J. B. Dalton and C. L. Schmidt, *J. Biol. Chem.*, 1933, **103**, 549–578.
41 T. Lee and Y. K. Lin, *Cryst. Growth Des.*, 2010, **10**, 1652–1660.
42 K. Nakamoto and A. E. Martell, *J. Chem. Phys.*, 1960, **32**, 588–597.
43 J. Zhou, X. Li, L. Yang, S. Yan, M. Wang, D. Cheng, Q. Chen, Y. Dong, P. Liu and W. Cai, *Anal. Chim. Acta*, 2015, **899**, 57–65.
44 C. Ziejewska, A. Grela and M. Hebda, *Materials*, 2023, **16**, 2044.
45 B. C. Eu and M. Al-Ghoul, *Chemical Thermodynamics: Reversible and Irreversible Thermodynamics*, World Scientific, 2017.
46 M. Dayeh, M. Ammar and M. Al-Ghoul, *RSC Adv.*, 2014, **4**, 60034–60038.
47 M. Al-Ghoul and R. Sultan, *Phys. Rev. E*, 2019, **100**, 052214.